

# Numerical Investigation of Conductivity Additive Dispersion in High-Power and High-Energy NMC-Based Lithium-Ion Battery Cathodes: Application-Based Guidelines

Anshuman Chauhan\* and Hermann Nirschl

Herein, guidelines are provided for the dispersion of conductivity additive in nickel-manganese-cobalt-oxide-based lithium-ion battery (LIB) cathodes with respect to its influence on electrochemical performance. The contrasting design strategies and operating conditions applicable to high-power and high-energy cathodes lead to significant differences in performance limiting factors for the respective microstructures. Hence, a generalization of the optimum dispersion of the conductivity additive that enhances cell performance in all cases is not possible. In this work, four distinct distributions of conductivity additive agglomerate/aggregate sizes resulting from varying mixing conditions are investigated with respect to their compatibility with cathode microstructures intended for different LIB applications with the help of spatially resolved electrochemical simulations. It is found that in the case of high-power cathodes, wherein ionic transport is the dominant performance limiting factor, a more significant proportion of agglomerates that are bigger in size leads to improved diffusion and intercalation conditions. Conversely, in the case of high-energy electrodes wherein the conductivity additive content is minimized, a larger fraction of smaller aggregates, produced by the fragmentation of the agglomerates during the mixing process are essential to ensure sufficient electrical conductivity.

to shape the future of mobility in form of electric vertical takeoff and landing (eVTOL) aircrafts. Although LIBs are a versatile energy-storage medium with higher energy density and rate capability compared to their counterparts, there is a need to develop LIBs tailored to specific application to meet the requirements of the future. For instance, LIBs to be used in electrical vehicles intended for greater range per charge must fulfill higher energy requirements; in contrast, higher rate capability is essential for an eVTOL that requires considerably higher power at takeoff and landing. Since energy density in LIBs is often won at the cost of rate capability and in turn power density, cell manufacturers must choose between the two during the conception of cell design for a given application. An overview of the key decisions to be made in this process has been highlighted by Lain et al.<sup>[3]</sup> At the cathode level, a high-energy cell differs from a high-power cell in that, it has higher coat weights with a higher mass ratio of active material thus resulting

## 1. Introduction

Owing to the need of the hour to progress toward renewable energy sources, recent years have seen rapid electrification of the industrial<sup>[1]</sup> and transportation<sup>[2]</sup> sector. Lithium-ion batteries (LIBs) are at the forefront of this global transition. The field of application of LIBs already spans from consumer electronics to electric vehicles as well as power tools and is expanding steadily

in larger thickness and lower porosity. Furthermore, high-energy cathodes constitute significantly lesser proportions of the conductivity additive and binder as compared to a high-power cathode. The contrasting design strategies involved in the construction of cathodes as well as the intended operation conditions for respective applications lead to significantly different microstructural properties and limiting mechanisms. In case of high-energy electrodes, the electrical conductivity possesses as the limiting factor owing to the high insulating active material and low conductive additive content. Since the rate capability of high-energy cathodes is low,<sup>[4]</sup> the cathodes are operated under C-rates at which the ionic diffusion is usually sufficient. On the contrary, high-power cathodes usually possess abundant conductivity additive to ensure adequate electrical connection within the electrode but the ionic conductivity is the limiting factor because of the necessity of faster ionic diffusion at higher C-rates.

The extensive review on the manufacturing research in the field of LIBs<sup>[5]</sup> clearly highlights the potential of manufacturing processes in shaping the resulting microstructure of LIB electrodes and hence their performance. Furthermore, numerous theoretical and experimental attempts have been made by

A. Chauhan, H. Nirschl  
Institute of Mechanical Process Engineering and Mechanics  
Karlsruhe Institute of Technology  
Kaiserstrasse 12, 76131 Karlsruhe, Germany  
E-mail: anshuman.chauhan@kit.edu

 The ORCID identification number(s) for the author(s) of this article can be found under <https://doi.org/10.1002/ente.202300281>.

© 2023 The Authors. Energy Technology published by Wiley-VCH GmbH. This is an open access article under the terms of the Creative Commons Attribution License, which permits use, distribution and reproduction in any medium, provided the original work is properly cited.

DOI: 10.1002/ente.202300281

research groups worldwide to unravel the influence of individual manufacturing processes on the resulting electrodes. In chronological order of cell manufacturing, dry as well as wet mixing was investigated by Bockholt et al.<sup>[6,7]</sup> and Bauer et al.,<sup>[8]</sup> followed by studies on dispersion by Mayer et al.<sup>[9]</sup> and Dreger et al.<sup>[10,11]</sup>. Subsequently, the influence of drying was reported by Lombardo et al.<sup>[12]</sup> and Lippke et al.<sup>[13]</sup>. Finally, Ngandjong et al.<sup>[14]</sup> and Primo et al.<sup>[15]</sup> delivered insights into calendaring in their studies. To overcome the inherent shortcomings of high-power and high-energy cathode cell design, manufacturing processes must be manipulated to achieve optimized microstructures. In case of high-energy cathodes, this implies achieving improved electrical conductivity without significant loss in ionic transport and an enhanced ionic conduction alongside the established electrical network for high-power cathodes. This prospect was exploited by researchers in the recent years. Kremer et al.<sup>[16]</sup> were able to show that low drying rates could improve the rate capability of high-energy thick electrodes. Gottschalk et al.<sup>[17]</sup> reported the improvement in the performance of LIB anodes by means of a two-layered microstructure.

In this work, computational investigations have been carried out to determine the degree of dispersion of the conductivity additive best suited for high-energy and high-power cathode application respectively. The basis of the dispersion degree, indicating the progress of deagglomeration of the conductivity additive in the dispersion step of cathode manufacturing, is formed by the study on the quality control of LIB electrode suspensions.<sup>[10]</sup> The different degrees of dispersion investigated in this work are characterized by size distribution of the conductivity additive measured after dry mixing with the active material at different tip speeds of the mixing device.<sup>[18]</sup> The measurements were made at the Institute for Particle Technology, Technische Universität Braunschweig, and kindly made available by Dr.-Ing. Julian Mayer. All the size distributions measured at different mixer tip speeds of 2.5, 6.25, 9.5, and 13 ms<sup>-1</sup> possess a bimodal shape wherein the peak at higher size indicates the population of agglomerates in the mixture and the peak at smaller sizes that of the fragmented agglomerates and aggregates. However, with rising tip speeds, the peak of the agglomerates diminishes and the population of the aggregates and smaller fragments rises. To realize the change in microstructure that would result from such deagglomeration during mixing the measured size distributions were incorporated into idealized cathode geometries<sup>[19]</sup> intended for numerical investigations. The idealized geometries generated for the purpose of this work are composed of the active component, lithium nickel manganese cobalt oxide (NMC), and the passive component, comprising the conductivity additive and the binder modeled as smooth spheres. Depending on the chosen application, the idealized microstructures were modeled to replicate different mass loading and hence thickness, porosity, and composition based on the respective recipe. Eventually, all the generated microstructures were transformed into half-cell domains with the addition of an electrolyte region and periodic boundaries in the in-plane direction followed by characterization of these individual domains by means of numerical determination of structural parameters namely effective electrical conductivity, tortuosity, and specific available active surface area. Finally, the entire half-cell domain was subjected to galvanostatic operation condition at discharge rate suitable for the respective application to obtain potential progression with respect

to a lithium-metal anode to be used consecutively for the evaluation of performance. The insights gained have been presented as guidelines for cell design keeping in mind the intended application.

## 2. Numerical Method

### 2.1. Idealized Microstructure Generation

The idealized cathode geometries investigated in this contribution were generated by means of the open-source particle simulation software LIGGGHTS made available by the CFDEM project.<sup>[20]</sup> Hereby, discrete element method (DEM) simulations were carried out to generate particulate assemblies capable of replicating LIB cathode microstructure. The idealized aspect of the resulting geometries lies in the fact that all the particles are assumed to be dense, smooth spheres. For all particle simulations carried out within the framework of this work, two types of particles were used, namely the active material particle representing the NMC particle and the carbon binder domain (CBD) particle representing a combination of the conductivity additive carbon black and binder polyvinylidene difluoride. It was assumed that carbon black and the binder exist in equal quantities in all the recipes and that all of it was absorbed by carbon black, leaving no surplus binder that could attach itself to the active material surface. It is to be noted that such a scenario is not achievable with the contemporary manufacturing methods involved in the mass production of LIBs. However, Bauer et al.<sup>[8]</sup> showed that a dry mixing pretreatment of the active material with carbon black followed by dispersion in binder–solvent solution along with additional carbon black to immobilize the binder could achieve the assumed state. Since NMC particles exhibit a rather narrow size distribution a constant diameter of 10 μm was assumed.<sup>[8]</sup> In contrast, size for the CBD particle was derived from the measured size distributions after dispersion for a constant amount of time and varies depending on the mixing tip speed as shown in **Figure 1**.

To calculate the number of particles of each constituent and its individual species in the particle simulations, at first the design for the respective application was determined. In case of high-power cathodes, a recipe (active-material:carbon-black:binder wt%) of 90:5:5 wt% was chosen which was transformed into a half-cell computational domain of dimension 20 × 20 × 40 μm with a porosity of 40%. Whereas, for high-energy cathode 98:1:1 wt% was the chosen recipe. The computational half-cell domain in case of the latter has a dimension of 20 × 20 × 120 μm and a porosity of 30%. Based on these design parameters, the volume fraction of the components in the half-cell computational domain could be calculated based on the method applied by Hein et al.<sup>[21]</sup>. Depending on the chosen recipe, the density of the resulting solid cathode  $\rho_c^s$  can be calculated with the relation

$$\rho_c^s = \frac{1}{\sum_i \frac{w_i}{\rho_i}} \quad (1)$$

wherein  $w_i$  represents the mass fraction of the constituent particle type, and  $\rho_i$  its density. Upon substituting the half-cell porosity into Equation (2), the volume fraction of the solid components  $\epsilon_c$  in the half-cell can be calculated using the half-cell porosity  $\epsilon$ .

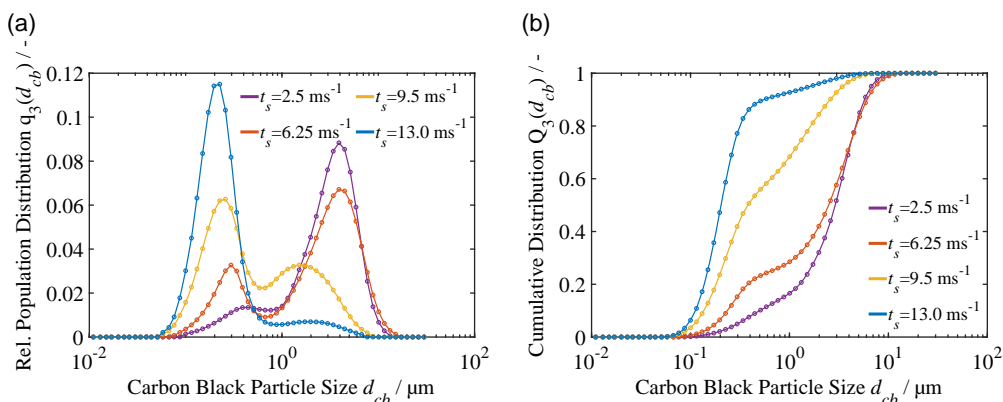


**Figure 1.** Measured carbon black particle size (courtesy Mayer et al.) represented as a) relative population distribution and b) cumulative distribution.

$$\varepsilon_c = 1 - \varepsilon \quad (2)$$

Finally, Equation (3) reveals the volumetric fraction of the constituent particles in the half-cell and Equation (4) reveals the number of particles  $n_{i,j}$  of the individual species of a given constituent. Herein,  $V$  denotes the total half-cell volume  $L \times B \times H$  and  $q_3(d_{i,j})$  denotes the diameter-dependent relative population of a species  $j$  belonging to a given constituent  $i$ .

$$\varepsilon_i = \frac{w_i}{\rho_i} \times \rho_c^s \times \varepsilon_c \quad (3)$$

$$n_{i,j} = \frac{6 \times V \times \varepsilon_i \times q_3(d_{i,j})}{\pi \times d_{i,j}^3} \quad (4)$$

Following the determination of the quantity of the constituents and their respective species, these were inserted randomly into a simulation box much larger than the intended half-cell size in the framework of the software LIGGGHTS as illustrated by the *initial suspension* state in **Figure 2**. Subsequently, the simulation box was made to shrink to a given dimension ensuring constant rate of shrinkage followed by relaxation to overcome the resulting overlapping between the particles. The simplified Johnson–Kendall–Roberts (SKJR) model<sup>[22]</sup> was used to mimic the cohesion between the particles, and their movement was dictated by the conservation of momentum. Additionally, contact force between the particles was modeled by the Hertz–Mindlin model.<sup>[23]</sup> This simulation step was intended to imitate the drying process. Conclusively, the particle assembly was subjected to

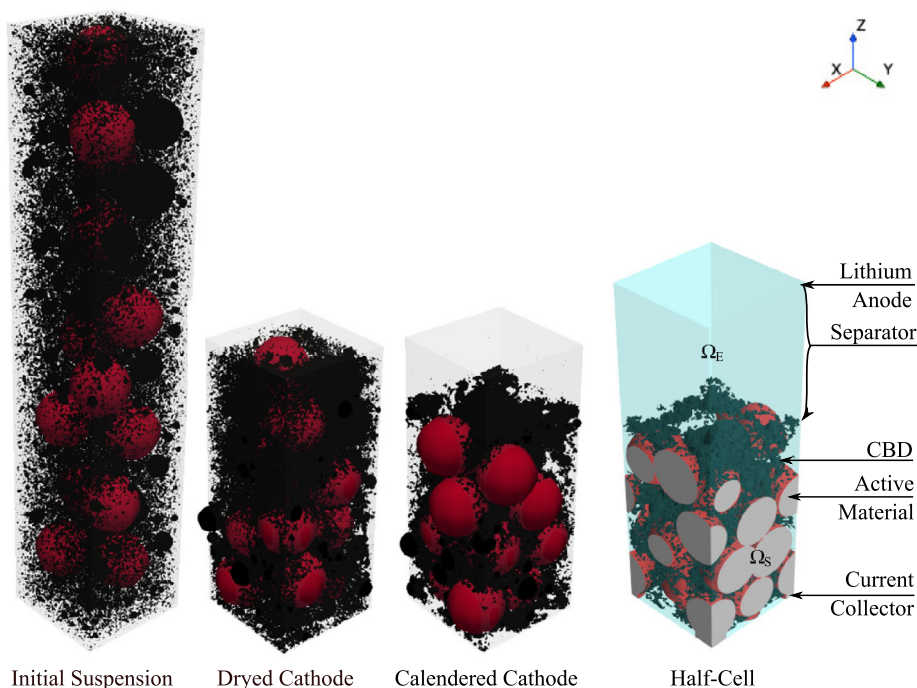


**Figure 2.** Generation of idealized half-cell geometries.

**Table 1.** Material properties and proportions of the cathode constituents.

	Active material	Carbon black	Binder
Density [kg m <sup>-3</sup> ]	4780	1850	1780
High-power cathode weight [%]	90	5	5
High-power cathode volume [%]	46	7	7
High-energy cathode weight [%]	98	1	1
High-energy cathode volume [%]	66	2	2

uniaxial compression until the predetermined thickness of the cathode based on the respective application was reached, with a fixed wall moving at a constant speed following the calendaring process. The chain of DEM simulations thus executed are only intended as means of generating a spatial distribution of cathode components similar to LIB cathodes. Since, the initial insertion of the particles into the simulation box is random, the resulting spatial distribution of the CBD is homogeneous and effects such as binder migration during drying are not accounted for. Detailed description of the particle–particle as well as particle–wall interaction necessary to describe the transient behavior of cathode slurries are therefore out of the scope of this work. The resulting volume and weight fractions as well as the used material properties are summarized in **Table 1**. Since carbon black and binder have been modeled as composite particle, its volume and weight fraction are the sum of the value for carbon black and binder. To transform the particulate assemblies resulting from the previously elaborated DEM simulations into half-cell computational domain, at first these were extended periodically.<sup>[19]</sup> Subsequently, to prepare the particulate assemblies for meshing in Simcenter STAR-CCM+,<sup>[24]</sup> the point contacts between the particle were treated by means of the surface wrapper utility.<sup>[25]</sup> Herein, points on the surfaces of particles closer than a predefined size were bridged together to form a sort of wrap over the entire assembly. This leads to an addition of mass to the cathode structure; however, the change made in the volume fraction of the respective components and the porosity was negligible. The wrapped structure was then trimmed to the dimension of the half-cell resulting in the domain  $\Omega_S$ . Finally, after the inclusion of the electrolyte domain  $\Omega_E$  in the pores and in the separator domain on the top, the half-cell computational domain was forged as shown on the far right in Figure 2. A total of eight idealized half-cell domains were constructed. A set of four, for each application corresponding to the different tip speeds.

## 2.2. Characterization

The interplay of conduction phenomenon strongly effects the performance of LIBs. The electric and ionic conductivities are interdependent and determined by the cathode microstructure. In this contribution, effective microstructural properties related to these conduction phenomenon were evaluated by a numerical method developed by Kespe et al.<sup>[26]</sup> The generalized form of the equation set utilized is summarized in **Table 2**. The numerical method utilizes the law of conservation as is stated by Equation (2.1) in the Table. Herein,  $\psi$  represents concentration  $c$  in case of

**Table 2.** Model equations for determination of effective microstructural properties.

$\Omega = \Omega_S \cup \Omega_E, \partial\Omega = \partial\Omega_B \cup \partial\Omega_{S,E} \cup \partial\Omega_P \cup \partial\Omega_T$	–
$\nabla \cdot (\alpha \cdot \nabla \psi) = 0$	(2.1)
$\nabla \psi \cdot \vec{n} = 0$ on $\partial\Omega_{S,E}$	(2.2)
$\vec{i} = \alpha \cdot \nabla \psi$	(2.3)
$\alpha^{\text{eff}} = \frac{\vec{i} \partial\Omega \times H}{\Delta\psi \times \Delta x \times \Delta y}$	(2.4)

mass conservation and potential  $\phi$  in case of charge conservation. The spatially dependent coefficient  $\alpha$  represents diffusion coefficient  $D_E$  for the former and electrical conductivity  $\kappa_S$  for the latter. To evaluate the effective value of  $\alpha$  for the microstructure, a unit gradient  $\Delta\psi$  was applied across the extremities ( $\partial\Omega_B$  and  $\partial\Omega_T$ ) of the respective domains. The electrical conductivity is restricted to the cathode region  $\Omega_S$ , while the ionic conduction occurs only within the electrolyte in the region  $\Omega_E$ . Due to the applied gradient, a flux  $\vec{i}$  evolves across the microstructure. The flux is limited to the respective domain by the boundary condition 2.2 at the contact boundary between cathode and electrolyte  $\partial\Omega_{S,E}$ . Furthermore, the periodic boundaries  $\partial\Omega_P$  in the direction perpendicular to the flux ensure that the investigated domain is representative. To determine the effective property, formula 2.4, derived from Equation (2.1) and (2.3) was used. Herein,  $H$  represents the thickness of the domain, and  $\Delta x$  and  $\Delta y$  represent the lateral dimensions. The formulation of  $\Delta\psi$  depends on the evaluated property, that is,  $(c_T - c_B)$  for mass and  $(\phi_T - \phi_B)$  for charge. The obtained effective electrical conductivity  $\kappa_S^{\text{eff}}$  is directly used as an indicator for the conductive capabilities of the cathode. However, for ionic conductivity, the chosen parameter is tortuosity  $\tau$ . Tortuosity is a dimension less factor indicating the quality of 3D pore system.<sup>[27]</sup> It interlinks porosity and diffusion phenomenon following the relation<sup>[28]</sup>

$$D_E^{\text{eff}} = D_E \frac{\varepsilon}{\tau} \quad (5)$$

A higher tortuosity is thus an indicator of poor quality with respect to ionic diffusion due to the lower effective diffusion coefficient  $D_E^{\text{eff}}$  at a given porosity. Another important microstructural property that has a significant influence on the half-cell performance is the available specific active surface area  $S_p$ . The electrochemical activity in a cell owing to the redox reactions is a surface phenomenon hence its availability effects the rate as well as the efficiency of these reactions. The dispersion and distribution of the inactive components namely carbon black and binder during the fabrication process strongly influence the availability of the active surface, since these components latch on to the active material surface they restrict movement of the lithium ion to an otherwise potential site of intercalation. In this work, the combination of carbon black and binder are considered to be dense; hence, no ionic diffusion is permitted through it. Numerous contemporary studies<sup>[12,21,29]</sup> have modeled the CBD to be porous with the help of effective ionic diffusion subjected to an assumption of intrinsic properties of the CBD such

as tortuosity and porosity. However, Mayer et al.<sup>[30]</sup> showed in their latest work that inner porosity of carbon black has an immense effect on the electrochemical properties of the electrode and the measurements required to make accurate estimation of the former are nontrivial. Furthermore, in their review of the modeling of inactive materials in LIBs, Chouchane et al.<sup>[31]</sup> noted that the completely restricted ionic diffusion through the

CBD was still able to replicate the spatial distribution of intercalated lithium in the electrode adequately and that, it was essential to account for the loss of active surface area. Therefore, the choice of completely restricted ionic diffusion was opted to build a worst-case scenario analysis. The specific active surface area available for intercalation per unit volume of the cathode is thus expressed as

$$S_V = \frac{\text{Total Active Surface Area} - \text{Active Surface Area occupied by the CBD}}{\text{Cathode Volume}} \quad (6)$$

### 2.3. Performance Evaluation

The spatially resolved 3D microstructural model proposed by Kespe et al.<sup>[32]</sup> was used as the basis for half-cell performance evaluation in this work. This model makes use of mass and charge balance equations to model the transport of lithium ions and electrons within the half cell. The generalized forms of these balances are stated as Equation (7) and (8). Herein,  $c$  represents the concentration,  $t$  the time,  $\vec{n}$  material flow, and  $\vec{i}$  the current.

$$\frac{\partial c}{\partial t} = -\nabla \cdot \vec{n} \quad (7)$$

$$\nabla \cdot \vec{i} = 0 \quad (8)$$

The computational domain of the model consists of two non-overlapping domains  $\Omega_S$  and  $\Omega_E$ . The material and current flux for the individual regions are summarized in **Table 3**. The solid domain  $\Omega_S$  can be further classified into the active domain  $\Omega_S^{\text{AM}}$  and the passive domain  $\Omega_S^{\text{CBD}}$ . Likewise, the electrolyte domain is classified into  $\Omega_E^{\text{SEP}}$  and  $\Omega_E^{\text{REST}}$  such that the former represents the separator domain within the electrolyte, modeled with the help of effective properties following the relation 5 and the latter the remaining electrolyte region. In case of the solid region, the electrical conductivity is set in such a manner that  $\kappa_S^{\text{CBD}} \gg \kappa_S^{\text{AM}}$  to model the superior electrical conductivity of the passive material. Conversely, to limit the lithium transport in the passive region the diffusion coefficient have been chosen such that  $D_S^{\text{CBD}} \ll D_S^{\text{AM}}$ . In contrast, for the electrolyte region, the electrical conductivity  $\kappa_E$  and the diffusion coefficient  $D_E$  have been modeled to depend on the electrolyte concentration following the relations 9 and 10. These relations are based on the parameterization published by Less et al.,<sup>[33]</sup> wherein the liquid electrolyte is modeled as a completely dissociated conducting salt, lithium hexafluorophosphate (LiPF<sub>6</sub>) in a solvent consisting of a mixture of ethylene carbonate and ethyl methyl carbonate.

$$\kappa_E = -2.39 \times 10^{-11} \times c_E^4 + 1.21 \times 10^{-7} \cdot c_E^3 - 2.89 \times 10^{-4} \times c_E^2 + 0.32 \times c_E - 2.789 \quad (9)$$

**Table 3.** Mass and current flux in cathode and electrolyte domain.

Cathode, $\Omega_S = \Omega_S^{\text{AM}} \cup \Omega_S^{\text{CBD}}$	Electrolyte, $\Omega_E = \Omega_E^{\text{REST}} \cup \Omega_E^{\text{SEP}}$
$\vec{n}_S = -D_S(\vec{x}) \cdot \nabla c_S \quad (3.1)$	$\vec{n}_E = -D_E \cdot \nabla c_E + \frac{\rho}{F} \cdot \vec{i}_E \quad (3.2)$
$\vec{i}_S = \kappa_S(\vec{x}) \cdot \nabla \phi_S \quad (3.3)$	$\vec{i}_E = -\kappa_E \cdot \nabla \phi_E - \frac{2RT\kappa_E}{F} (1 - t_0^+) \nabla \ln c_E \quad (3.4)$

$$D_E = 1.2 \times 10^{-21} \times c_E^4 - 6.5 \times 10^{-18} \times c_E^3 + 1.14 \times 10^{-14} \times c_E^2 - 8.06 \times 10^{-12} \times c_E + 2.24 \times 10^{-9} \quad (10)$$

At the interface between the two nonoverlapping regions  $\partial\Omega_{S,E}$ , a Butler–Volmer-type relation dictates the kinetics of the electrochemical reactions via the intercalation current density  $\vec{i}_{\text{BV}}$ .<sup>[34]</sup> Under consideration of symmetry, this relation can be stated as Equation (11). Hereby, the intercalation current density is set to zero on the passive subdomain  $\partial\Omega_{S,E}^{\text{CBD}}$  to ensure its inactivity in the intercalation reaction. The universal constants in the equation are  $F$  Faraday's constant and  $R$  universal gas constant. In addition,  $\eta$  denotes the overpotential determined by Equation (12), where the equilibrium potential  $U_{\text{eq}}$  of NMC-622 in dependence to concentration is given by the polynomial function 13.<sup>[16]</sup>

$$\vec{i}_{\text{BV}} = \begin{cases} 2 \cdot k_{\text{BV}} (c_S^{\text{max}} - c_S)^\alpha (c_S)^\alpha (c_E)^\alpha \sinh\left(\frac{F}{2RT} \eta\right) & \text{on } \partial\Omega_{S,E}^{\text{AM}} \\ 0 & \text{on } \partial\Omega_{S,E}^{\text{CBD}} \end{cases} \quad (11)$$

$$\eta = \phi_S - \phi_E - U_{\text{eq}} \quad (12)$$

$$U_{\text{eq}} = 13.4905 - 10.96038 \times c_S + 8.203617 \times c_S^{1.358699} - 3.10758 \times 10^{-6} \times e^{(127.1216 \cdot c_S - 114.2593)} - 7.033556 \times c_S^{-0.03362749} \quad (13)$$

For both the regions, the material and charge transfer are coupled over the periodic boundaries in the in-plane direction. This ensures the applicability of the numerical results obtained at the microscale to the macroscale of the LIB cathode. Finally, the top of the electrolyte region in the half-cell as shown in Figure 2 was modeled to be composed of metallic lithium. On the other end of the half-cell, the cathode current collector was modeled to impose galvanostatic boundary conditions, such that a constant current flows through it. In case of high-power cathodes, a high discharge rate of 5 C was chosen and in case of high-energy cathodes the discharge rate was set to 0.5 C. To ensure charge neutrality, the condition 14 was assumed. Additionally, isothermal operation at  $T = 298$  K was assumed.

$$\vec{i}_{\text{BV}} \cdot \vec{n}_S = -\vec{i}_E \cdot \vec{n}_E \quad (14)$$

The measure of performance chosen for this contribution is the utilizable capacity of the half-cell. This performance parameter can be derived from the half-cell potential evaluated from the spatially resolved model with respect to the lithium-metal anode. In doing so, the half-cell potential at the cathode current collector is plotted along the depth of discharge (DOD). Evaluation of DOD is carried out based on the maximum theoretical lithium concentration  $c_{S,max}$ , the reference concentration at the beginning of galvanostatic discharge  $c_{S,ref}$ , and the concentration at given instance  $c_S(\vec{x}, t)$  following Equation (15).

$$DOD = \frac{\int (c_S(\vec{x}, t) - c_{S,ref})}{\int (c_{S,max} - c_{S,ref})} \quad (15)$$

Consequently, the depth of discharge achieved by the half-cell at the cutoff defined by the cutoff voltage, COV in comparison to the theoretically possible discharge evaluated under equilibrium conditions gives its utilizable capacity as stated by Equation (16).

**Table 4.** Parameters for the spatially resolved electrochemical model on the microscale.

	Value	Unit	Reference
<b>Cathode</b>			
Active material electrical conductivity $\kappa_S^{AM}$	1	$S\ m^{-1}$	[37]
CBD electrical conductivity $\kappa_S^{CBD}$	100	$S\ m^{-1}$	[35]
Active material coefficient of diffusion $D_S^{AM}$	$4.3032 \times 10^{-14}$	$m^2\ s^{-1}$	[16]
CBD coefficient of diffusion $D_S^{CBD}$	$1 \times 10^{-20}$	$m^2\ s^{-1}$	[26]
Initial cathode potential $\phi_{S,ref}$	4.3	V	[21]
Active material initial lithium concentration $c_{S,ref}^{AM}$	18409.57	$mol\ m^{-3}$	[16]
Active material maximum lithium concentration $c_{S,max}^{AM}$	50 451	$mol\ m^{-3}$	[16]
CBD lithium concentration $c_{S,ref}^{CBD}$	0	$mol\ m^{-3}$	[26]
<b>Electrolyte</b>			
Initial electrolyte potential at anode surface $\phi_{E,ref}$	0	V	[21]
Transfer number $t_+^0$	0.4	–	[33]
Initial lithium concentration $c_{E,ref}$	1000	$mol\ m^{-3}$	[26]
<b>Separator</b>			
Porosity $\epsilon_{sep}$	0.5	–	[26]
Tortuosity $\tau_{sep}$	1.5	–	[26]
<b>Butler–Volmer kinetics</b>			
Butler–Volmer reaction rate constant $k_{BV}$	$1.4693 \times 10^{-6}$	$A\ m^{-2.5}\ mol^{-1.5}$	[16]
Cathodic apparent transfer coefficient $\alpha_c$	0.5	–	[16]
Anodic apparent transfer coefficient $\alpha_a$	0.5	–	[16]

The complete set of parameters used in the spatially resolved model are summarized in Table 4.

$$UC = \frac{DOD(COV)}{DOD_{eq}(COV)} \times 100 \quad (16)$$

### 3. Results and Discussion

In the following studies for each application type, the half-cell variants were constructed to the same dimension and composition, as discussed in the previous section. The only factor that leads to difference in the half-cell microstructure is thus the chosen CBD dispersion dependent on the measurements made after a constant time in a mixer with changing tip speeds. The size distribution of the conductivity additives resulting from such a dispersion process typically has a bimodal form. Mayer et al.<sup>[9]</sup> describe modes of these distributions as the aggregate and agglomerate peak respectively for the smaller and larger particles. In this context, the term agglomerate refers to clusters held together by weak forces of attraction and aggregates as particulate structures held together by considerably stronger forces, that form the building blocks of agglomerates. As can be observed from Figure 1a, increase in tip speed leads to a shift of agglomerate peak into the aggregate peak. However, Mayer et al. showed in their study that, the median of the particle size obtained was independent of the tip speed and correlated closely with the total specific energy input into the mixer. Consequently, since higher tip speeds can deliver high energy in shorter time, smaller particle size can be attained from the shorter mixing time. Within in the frame of this work, the resulting size distributions have been extracted from measurements after constant mixing time. Hence, the focus of this contribution is to formulate guidelines on how particle-size distribution influences performance.

#### 3.1. High-Power Cathodes

Figure 3 shows the investigated domain of the high-power cathodes. As can be seen from the figure, the dispersion of the CBD at  $13\ ms^{-1}$  is much more pronounced than that at  $2.5\ ms^{-1}$ . This leads to significant differences in the half-cell microstructure. These differences were quantified by the characterization simulations elaborated in Section 2.2, the results of which are plotted in Figure 4. It can be observed from Figure 4a that the available specific active surface area shows a drastic drop from the  $2.5\ ms^{-1}$  variant to the  $6.25\ ms^{-1}$  variant followed by the convergence to a fairly constant value with rising tip speed. This is due to the fact that as the aggregate peak rises due to the increasing number of smaller particles resulting from the deagglomeration as shown in Figure 1a, numerous new contacts are formed between the fragmented CBD and the active material. These contact areas are considered to be fully blocked for lithium ions and hence a loss of active surface area is observed. Upon further increase in the aggregate peak with the tip speed no significant rise in these contacts can be inferred from the unchanged available surface. The increasing number of inter- as well as intra-particle contacts also has significant consequences for the conduction phenomenon. As can be seen from the Figure 4b on the left axis, the tortuosity increases steadily

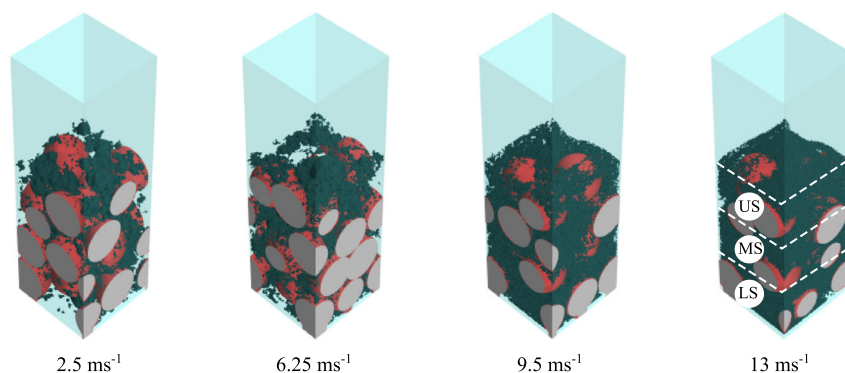


**Figure 3.** Idealized half-cell geometries of the high-power cathode variants.

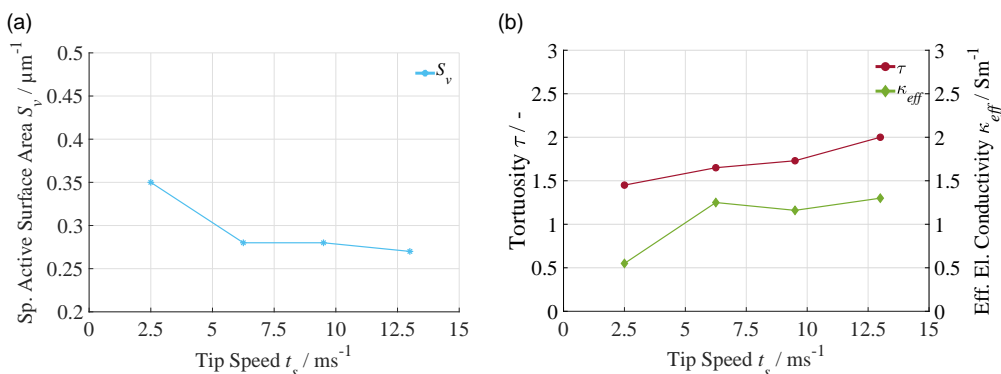


**Figure 4.** Structural characterization of the high-power cathode variants. a) Specific active surface area, b) tortuosity (left axis), and effective electrical conductivity (right axis).

with increasing tip speed leading to loss of ionic conductivity. Smaller CBD particles arising at higher tip speeds seep into the pore network of the half-cell thus breaching ionic conduction pathways and increasing tortuosity. In contrast, the increasing number of contacts associated with the smaller CBD particles lead to a considerable increase in the electrical conductivity from the 2.5 variant to the 6.25  $\text{ms}^{-1}$  variant, evident on the right axis in Figure 4b. Since, not all the new contacts formed owing to the increasing number of smaller particles contribute to the electrical network in the half-cell, no further relevant increase is noticed in the electrical conductivity with increasing tip speed. This, behavior is to be expected in percolating systems like the cathode suspension.<sup>[35]</sup>

Based on the results of the characterization simulations, it could be argued that larger CBD particle sizes present at low tip speeds could prove to be beneficial for high-power cathodes. Not only is the available specific active surface in these cases higher, but also the electrical conductivity percolation is already achieved at 6.25  $\text{ms}^{-1}$  and further increase of tip speed only leads to deterioration of the ionic conductivity. To bridge the gap between microstructural characteristics and half-cell performance and thereby verify this hypothesis, scale-resolving microstructural simulations were carried out as explained in Section 2.3. Since, the scale-resolving simulations are extremely time and cost intensive only the domain of the tip speed wherein relevant differences in microstructural properties were observed,

was investigated further. The half-cell potential recorded at the current collector of the half-cells during a 5C discharge with respect to pure metal anode is plotted against the depth of discharge in Figure 5a. It is evident from the figure that the half-cell variant at tip speed 2.5  $\text{ms}^{-1}$  exhibits higher half-cell potential across the entire depth of discharge than the 6.25  $\text{ms}^{-1}$  variant. Accordingly, the evaluated utilizable capacity of the former is superior to the latter as indicated in the figure. The reasons for this result can be elucidated by the steep difference in the available specific active surface area between the two variants. Higher surface area available for intercalation in case of the 2.5  $\text{ms}^{-1}$  leads to lower levels of intercalation current density across the cathode, this in turn leads to lower overpotential dictated by Equation (11), thereby improving utilizability. This was verified by the investigation of average intercalation current density presented in Figure 5b. Herein, the mean intercalation current density arising per unit area in three volumetrically equal regions of the cathode labeled as upper section (US), middle section (MS), and lower section (LS) in Figure 3 was evaluated from the scale-resolving simulations with respect to the global depth of discharge. As is evident, the lesser degree of dispersion for the 2.5  $\text{ms}^{-1}$  variant leads to higher available specific active surface area and hence lower intercalation current density in all the sections.

Another important inference that can be made from the Figure 5b is based on the progress of the average current density

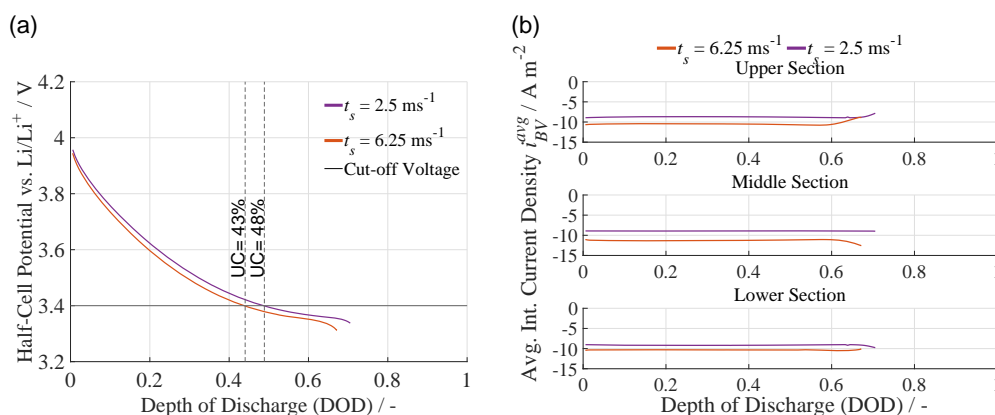


**Figure 5.** Performance evaluation of the chosen high-power cathode variants. a) Galvanostatic discharge curves at 5 C discharge rate; b) average intercalation current density in the upper section (US) (top), middle section (MS) (middle), and lower section (LS) (bottom).

with the depth of discharge. The magnitude of the average intercalation current density at beginning of the discharge is set based on the surface area of the respective sections and the distribution of the current dependent on the electrical conductivity. Only small differences in magnitude are observed, because on the one hand the sections poses similar surface area owing to the homogeneous distribution of the CBD, on the other hand the electrical conductivity is sufficiently high in all sections even in the case of the  $2.5 \text{ ms}^{-1}$  variant. Furthermore, since the thickness of the high-power cathode is small, a uniform distribution of the intercalation current results. Consequently, after a short duration of discharge at 80 s, no sharp gradients in the concentration distribution are visible for both the cathode and electrolyte domain in **Figure 6**. In this figure, the cathode and the electrolyte domain have been presented separately with labels for the respective concentration on the left and right side. Further, clipping planes at the midpoints in the lateral direction reveal the inside of the electrolyte domain. In contrast, toward the end of the discharge cycle at 400 s, the current at the US reduces at the expense of the other sections. This is seen most evidently for the  $6.25 \text{ ms}^{-1}$  variant in **Figure 5b**. Since, the total current in the half-cell must at all times be constant under galvanostatic

operation condition, this observation is an indication that the US gains concentration the fastest. The lithium ions originating at the anode are fed preferentially to the top layer of the cathode until the current density drops at  $\text{DOD} = 0.6$  owing to the rising surface concentration following the relation 11. This can be verified by the resolved representation of lithium concentration in the half-cell as shown in the **Figure 7**. As is evident in the figure, most prominently for the  $6.25 \text{ ms}^{-1}$  variant, the US shows the preferential accumulation of lithium concentration with the upper layer already exhibiting lithium concentration higher than 80% of the maximum solid concentration. This leads to the depletion of electrolyte also evident from the figure, from the growing black spots close to the current collector where the electrolyte concentration has dropped to 94% of the initial value, highlighting the inherent ionic conductivity limitation of high-power cathodes. However, numerous publications<sup>[16,32]</sup> have pointed out that this limitation could be countered by a favorable gradient in the distribution of the conductivity additive and binder in the thickness of the cathode. An increasing amount of binder and conductivity additive toward the cathode current collector without significantly influencing the local electrical conductivities of the individual section would enhance the ability of

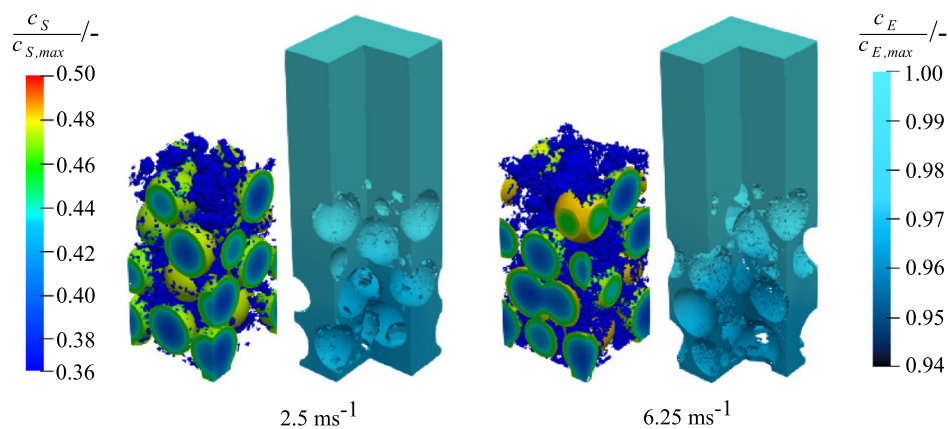


**Figure 6.** Relative lithium concentration distribution in the high-power cathode and electrolyte domain of the  $2.5 \text{ ms}^{-1}$  variant (left) and  $6.25 \text{ ms}^{-1}$  variant (right) after 80 s of galvanostatic discharge at 5 C.

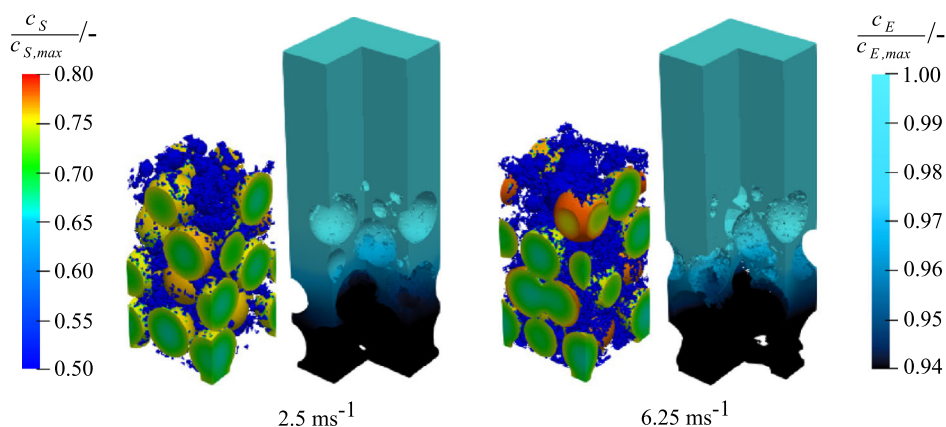


**Figure 7.** Relative lithium concentration distribution in the high-power cathode and electrolyte domain of the  $2.5 \text{ ms}^{-1}$  variant (left) and  $6.25 \text{ ms}^{-1}$  variant (right) after 400 s of galvanostatic discharge at 5 C.

the ions to navigate through the thickness of the half-cell hence improving the ionic conductivity without significant loss in the electrical conductivity. Hence conclusively, it is proposed that a lower degree of dispersion and an increasing gradient of the conductivity additive and binder in the direction of the current collector are best design choices for the high-power application.

### 3.2. High-Energy Cathodes

The investigated high-energy variants are shown in **Figure 8**. Similar to the previous subsection, a visible increase in the

fragmented CBD particles can be seen in the figure as the tip speed rises. However, the implications for the high-energy cathode are in sharp contrast to that for the high-power cathode, as can be seen from **Figure 9**. For all the characteristics, no significant change is observed up until the highest tip speed  $13 \text{ ms}^{-1}$ . At the highest tip speed ergo, the highest degree of dispersion however, a sharp drop in the available specific active surface area in **Figure 9a**, along with sharp increase in tortuosity and electrical conductivity in **Figure 9b** can be observed. These changes can be attributed to large fraction of smaller CBD fragments present in the microstructure similar to what was observed for the high-power variant. The onset of this change at much higher tip speed

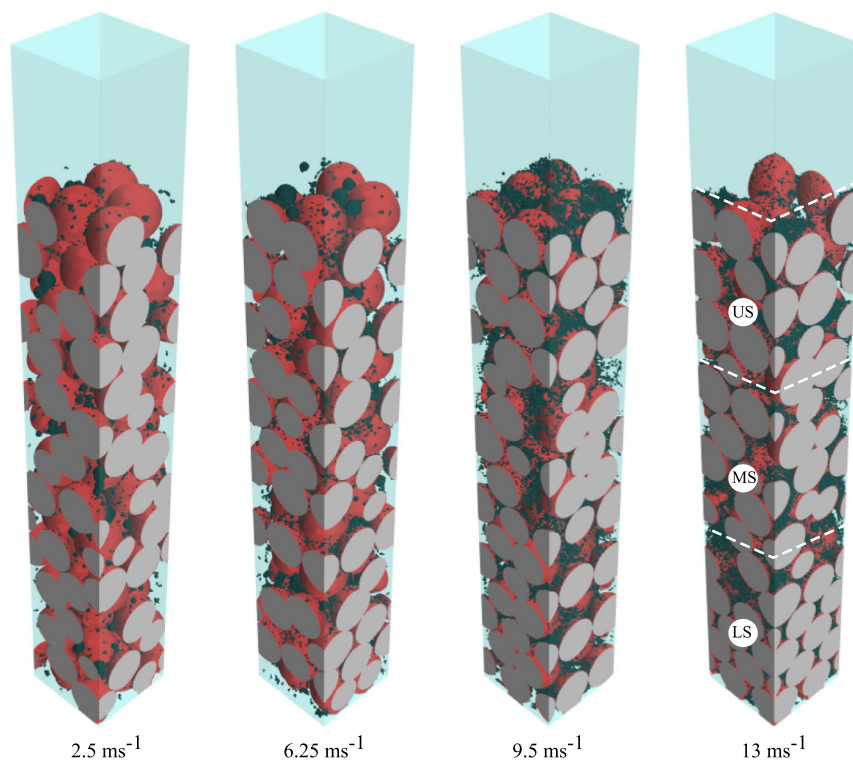


**Figure 8.** Idealized half-cell geometries of the high-energy cathode variants.

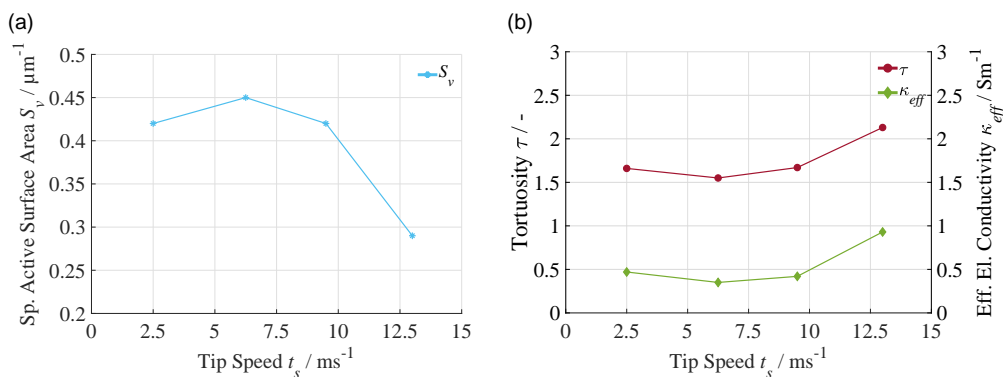


**Figure 9.** Structural characterization of the high-energy cathode variants. a) Specific active surface area, b) tortuosity (left axis), and effective electrical conductivity (right axis).

in case of the high-energy variant can be explained by their larger thickness hence longer conduction pathways, as well as significantly low CBD content. Thus, to significantly impact the characteristics of the high-energy cathode, a higher degree of dispersion is necessary. This additional effort however does not seem to be justified based on the results of characterization simulations. Although the electrical conductivity shows percolation behavior at the highest tip speed, the sharply increased number of contact responsible for it decreases the available surface area and increases the tortuosity immensely. The consequences of this change are evident in the half-cell potential curve extracted from the scale-resolving simulations. As shown in **Figure 10a**, despite the significantly better electrical conductivity of the  $13 \text{ ms}^{-1}$  variant, it is operating at similar half-cell potential as the  $6.25 \text{ ms}^{-1}$  variant. The cause here for being the considerably higher intercalation density present on its surface in all the sections of the cathode is evident from **Figure 10b**.

To seek deeper insights into the limiting mechanisms of both the variants, the concentration distribution in the half-cell during the discharge of the cathode variants at 0.5C was investigated. It is observed that in the starting stages of the discharge after 1200 s, a gradient in the lithium concentration develops close to the current collector for the  $6.25 \text{ ms}^{-1}$  variant as shown in **Figure 11**. This is due to the significantly lower electrical

conductivity present in the variant which in turn leads to high potential drop in the direction of the current collector. Since the region closer the current collector is operating at a lower potential in comparison to the other sections owing to the large potential drop over the thickness of the cathode, the overpotential in the LS is higher compared to the other sections and hence following the relation 11, it exhibits higher mean intercalation current density at the start of discharge. Consequently, the LS gains concentration the fastest and after a saturation at around  $\text{DOD} = 0.15$ , the current starts to drop at the expense of the other sections visible in **Figure 10b**. This behavior is not so evidently visible for the  $13 \text{ ms}^{-1}$  variant. Instead in this case, the disparity in potential of the cathode sections cannot be compensated with change in concentration owing to its considerably higher ionic limitation caused by the higher tortuosity.

The consequences of this become noticeable at the end stages of the discharge, at 6800 s. It can be seen in **Figure 12** that a lithium concentration gradient develops close to the separator for the  $13 \text{ ms}^{-1}$  variant. This is due to the sharp rise in tortuosity resulting from the smaller fragments of CBD present at high tip speeds. Since the conduction pathways for lithium ions are significantly longer in high-energy cell, this leads to drastic consequences for the high-energy cathode. The electrolyte starts to deplete close to the current collector at the LS of the half-cell as

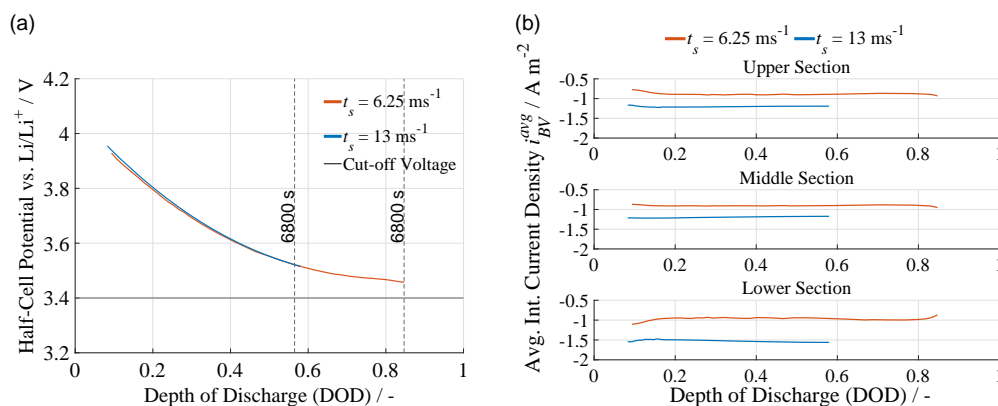


**Figure 10.** Performance evaluation of the chosen high-energy cathode variants. a) Galvanostatic discharge curves at 0.5C discharge rate; b) average intercalation current density in the US (top), MS (middle), and LS (bottom).

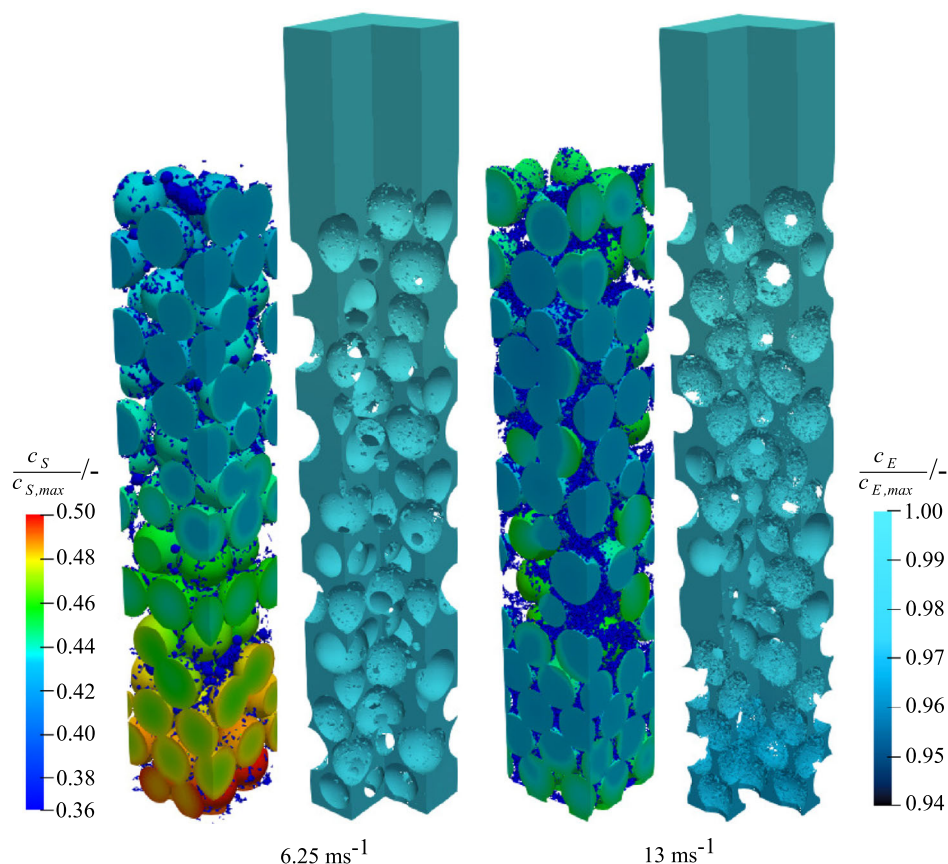


**Figure 11.** Relative lithium concentration distribution in the high-energy cathode and electrolyte domain of the  $6.25 \text{ ms}^{-1}$  variant (left) and  $13 \text{ ms}^{-1}$  variant (right) after 1200 s of galvanostatic discharge at  $0.5 \text{ C}$ .

lithium ions are not supplied fast enough from the anodic source. Furthermore, the discharge depth of the cathode is limited by the US. Thus, after 6800 s, it is only able to achieve a depth of discharge of around 0.57 whereas the  $6.25 \text{ ms}^{-1}$  variant reaches 0.84 in the same time, as indicated in Figure 10a. As expected, this behavior is absent in the  $6.25 \text{ ms}^{-1}$  variant at the end stages of discharge, where a concentration higher than 80% respective to the maximum value is seen along the entire thickness of the cathode in the figure on the left hand side. This is facilitated by further drop in the intercalation current for the variant, during the end stages in the bottom section as shown in Figure 10b. Since the limitation of the  $13 \text{ ms}^{-1}$  is already clear at this stage, further simulation up until the cutoff voltage to determine the utilizable capacity, requiring considerably higher computational effort due to low time step required specially at higher concentration were not carried out. Thus, it is evident that even at the highest degree of dispersion sufficient electrical conductivity has not been established warranting an increase in the CBD content. All the more, the increased tortuosity on account of the higher fragmentation of the CBD leads to diffusion limitation in the half-cell. To ensure a balance in the conduction phenomenon, it is proposed to consider higher CBD content than 1 wt% to ensure sufficient electrical conductivity at higher degree of dispersion. At the same time, similar to the case of high-power cathodes, a gradient in the distribution of

the CBD with increasing content in the direction of the current collector must be established to insure adequate mobility of the lithium ions. These observations are in accordance with the simulative predictions made by Kremer et al.<sup>[16]</sup> Finally, to preserve the available active surface area despite the higher degree of dispersion the shape of the conductivity additive could be exploited. It was found in numerous studies that conductive additives with higher aspect ratio (such as graphite)<sup>[35,36]</sup> exhibit much lower percolation threshold hence reducing the content of conductivity additive needed and therefore the active surface area blocked by the passive elements. Conclusively, it can be inferred that a higher degree of dispersion is necessary for the high-energy application to enable improvement in the electrical conduction, provided sufficient reach of the lithium ion through a favorable distribution of the conductivity additive and the use of conductivity additive enabling enhanced percolation is ensured.

#### 4. Conclusion

In the framework of this contribution, four different degrees of dispersion of the conductivity additive derived from measurements made after mixing of the cathode components for a constant time were investigated numerically. The contribution focuses on the suitability of these dispersion degrees for

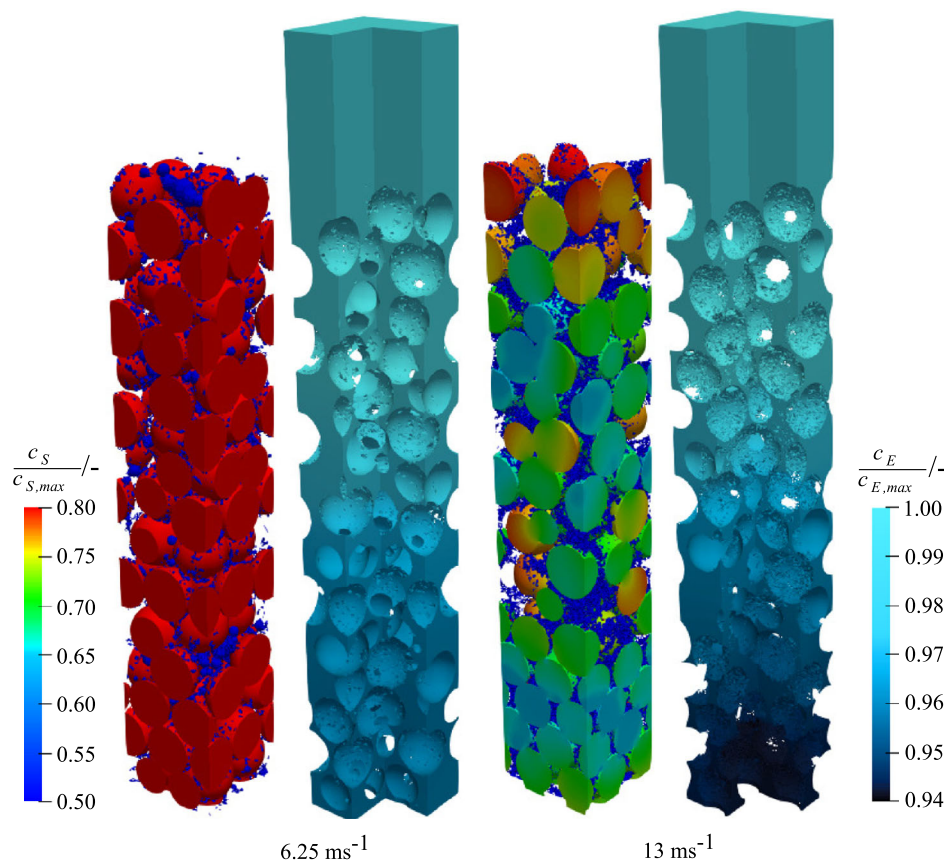


**Figure 12.** Relative lithium concentration distribution in the high-energy cathode and electrolyte domain of the  $6.25 \text{ ms}^{-1}$  variant (left) and  $13 \text{ ms}^{-1}$  variant (right) after 6800 s of galvanostatic discharge at 0.5 C.

contrasting applications of LIBs namely high power and high energy. The design parameters of the chosen applications and the guidelines derived from the investigations have been summarised in Table 5. In case of the high-power application, it was found that a lower degree of dispersion was adequate for the cathode design. The high CBD content in high-power cathode enabled sufficient electrical conduction even at the lowest degree of dispersion of the additive, and further vigorous

**Table 5.** Summary of the application-based design parameters and guidelines with respect to conductivity additive and binder in NMC-based lithium-ion battery cathodes.

	High power	High energy
Recipe (AM:CB:Binder) [wt%]	90:5:5	98:1:1
Thickness [ $\mu\text{m}$ ]	40	120
Porosity [%]	40	30
Inherent limitation	Ionic conduction	Electrical conduction
Degree of dispersion	Low, sufficient	High, necessary
Conductivity additive content	Sufficiently high	>1 wt%
Distribution	Increasing content toward CC	Increasing content toward CC

dispersion led to loss of specific active surface area and ionic conductivity. Moreover, a suggestion for distribution of the CBD in the thickness of the cathode such that more CBD content is present close to the current collector has been proposed as an additional measure for an optimal design to overcome the built-in shortcomings of these cathodes.

In contrast, in case of the high-energy application, it was observed that a higher degree of dispersion is essential to establish an electrical conduction network. This, however, comes at the cost of significant ionic limitation and loss of the active surface. The CBD content in high-energy cathodes must be high enough as well as dispersed well enough to connect the extremities of the cathode to the source of current at the current collector. Simultaneously, the CBD content and its distribution must be kept under check to avoid deterioration of the ionic conduction. Similar to the higher-power cathode, a distribution gradient in the CBD content with higher CBD close to the current collector would enable far reach of the lithium ions. Additionally, the CBD content needed to reach sufficient electrical conductivity could be kept under check by use of conductivity additives with a higher aspect ratio such as graphite. With these proposals, the presented work contributes to the microstructural optimization of the LIB cathode manufacturing and complements the research in the direction of application-tailored LIB manufacturing to cater to diverse demands of future electrification.

## Acknowledgements

The authors gratefully acknowledge the funding and support by the German Research Foundation (DFG—Deutsche Forschungsgemeinschaft) within the research training group SiMET under the project number DFG GRK2218/2. Additionally, the support by the state of Baden-Württemberg through bwHPC is highly acknowledged. Finally, the authors would like to thank Dr.-Ing. Julian Mayer, Institute for Particle Technology, Technische Universität Braunschweig, for sharing the experimental data.

Open Access funding enabled and organized by Projekt DEAL.

## Conflict of Interest

The authors declare no conflict of interest.

## Data Availability Statement

The data that support the findings of this study are available from the corresponding author upon reasonable request.

## Keywords

conductivity additives, dispersion, energy density, performance, power density

Received: March 17, 2023

Revised: April 6, 2023

Published online:

- [1] A. R. Quinteros-Condoretty, S. R. Golroudbary, L. Albareda, B. Barbiellini, A. Soyer, *Proc. CIRP* **2021**, 100, 73.
- [2] J. D. Dogger, B. Roossien, F. D. J. Nieuwenhout, *IEEE Trans. Energy Convers.* **2011**, 26, 256.
- [3] M. J. Lain, J. Brandon, E. Kendrick, *Batteries* **2019**, 5, 64.
- [4] M. Singh, J. Kaiser, H. Hahn, *J. Electrochem. Soc.* **2015**, 162, A1196.
- [5] P. S. Grant, D. Greenwood, K. Pardikar, R. Smith, T. Entwistle, L. A. Middlemiss, G. Murray, S. A. Cussen, M. J. Lain, M. J. Capener, M. Copley, C. D. Reynolds, S. D. Hare, M. J. H. Simmons, E. Kendrick, S. P. Zankowski, S. Wheeler, P. Zhu, P. R. Slater, Y. S. Zhang, A. R. T. Morrison, W. Dawson, J. Li, P. R. Shearing, D. J. L. Brett, G. Matthews, R. Ge, R. Drummond, E. C. Tredenick, C. Cheng, et al., *J. Phys: Energy* **2022**, 4, 042006.
- [6] H. Bockholt, W. Haselrieder, A. Kwade, *ECS Trans.* **2013**, 50, 25.
- [7] H. Bockholt, W. Haselrieder, A. Kwade, *Powder Technol.* **2016**, 297, 266.
- [8] W. Bauer, D. Notzel, V. Wenzel, H. Nirschl, *J. Power Sources* **2015**, 288, 359.
- [9] J. K. Mayer, L. Almar, E. Asylbekov, W. Haselrieder, A. Kwade, A. Weber, H. Nirschl, *Energy Technol.* **2020**, 8, 1900161.
- [10] H. Dreger, M. Huelsebrock, L. Froboese, A. Kwade, *Industr. Eng. Chem. Res.* **2017**, 56, 2466.
- [11] H. Dreger, W. Haselrieder, A. Kwade, *J. Energy Storage* **2019**, 21, 231.
- [12] T. Lombardo, A. C. Ngandjong, A. Belhacen, A. A. Franco, *Energy Storage Mater.* **2021**, 43, 337.
- [13] M. Lippke, T. Ohnimus, T. Heckmann, D. Ivanov, P. Scharfer, W. Schabel, C. Schilde, A. Kwade, *Energy Technol.* **2023**, 11, 2200724.
- [14] A. C. Ngandjong, T. Lombardo, E. N. Primo, M. Chouchane, A. Shodiev, O. Arcelus, A. A. Franco, **2021**, 485, 229320.
- [15] E. N. Primo, M. Chouchane, M. Touzin, P. Vazquez, A. A. Franco, *J. Power Sources* **2021**, 488, 229361.
- [16] L. S. Kremer, A. Hoffmann, T. Danner, S. Hein, B. Prifling, D. Westhoff, C. Dreer, A. Latz, V. Schmidt, M. Wohlfahrt-Mehrens, *Energy Technol.* **2020**, 8, 1900167.
- [17] L. Gottschalk, C. Oertel, N. Strzelczyk, J. Muller, J. Kruger, W. Haselrieder, A. Kwade, *Energy Technol.* **2022**, 11, 2200858.
- [18] E. Asylbekov, J. Mayer, H. Nirschl, A. Kwade, *Energy Technol.* **2022**, 11, 2200867.
- [19] A. Chauhan, E. Asylbekov, S. Kespe, H. Nirschl, *Electrochem. Sci. Adv.* **2022**, 3, 2100151.
- [20] C. Kloss, C. Goniva, A. Hager, S. Amberger, S. Pirker, *Progr. Comput. Fluid Dyn. Int. J.* **2012**, 12, 140.
- [21] S. Hein, T. Danner, D. Westhoff, B. Prifling, R. Scurtu, L. Kremer, A. Hoffmann, A. Hilger, M. Osenberg, I. Manke, M. Wohlfahrt-Mehrens, V. Schmidt, A. Latz, *J. Electrochem. Soc.* **2020**, 167, 013546.
- [22] K. Johnson, K. Kendall, A. D. Roberts, *Proc. Roy. Soc. Lond. A. Math. Phys. Sci.* **1971**, 324, 301.
- [23] R. D. Mindlin, *J. Appl. Mech.* **1949**, 16, 259.
- [24] Siemens Digital Industries Software, *Simcenter STAR-CCM+ User Guide v. 2021.1*, Version 2021.1, **2021**.
- [25] Siemens Digital Industries Software in *Surface Wrapping the Geometry*, Siemens, **2021**, pp. 3067, <https://docs.sw.siemens.com/documentation/external/PL20200805113346338/en-US/userManual/userguide/html/index.html#page/STARCCMP%2FGUID-71B2E016-A821-4778-8D4F-2268C8FC44B1.html%23>.
- [26] M. A. Kespe, in *Simulation Von Transportvorgängen in Lithium-Ionen Batterien Auf Der Partikulären Ebene*, Karlsruhe Institut für Technologie (KIT), Karlsruhe **2019**.
- [27] D. Kehrwald, P. R. Shearing, N. P. Brandon, P. K. Sinha, S. J. Harris, *J. Electrochem. Soc.* **2011**, 158, A1393.
- [28] E. E. Petersen, *AIChE J.* **1958**, 4, 343.
- [29] T. Danner, M. Singh, S. Hein, J. Kaiser, H. Hahn, A. Latz, *J. Power Sources* **2016**, 334, 191.
- [30] J. Mayer, H. Bockholt, A. Kwade, *SSRN Electron. J.* **2022**, <https://doi.org/10.2139/ssrn.3998841>.
- [31] M. Chouchane, A. A. Franco, *Energy Storage Mater.* **2022**, 47, 649.
- [32] M. Kespe, H. Nirschl, *Int. J. Energy Res.* **2015**, 39, 2062.
- [33] G. B. Less, J. H. Seo, S. Han, A. M. Sastry, J. Zausch, A. Latz, S. Schmidt, C. Wieser, D. Kehrwald, S. Fell, *J. Electrochem. Soc.* **2012**, 159, A697.
- [34] J. Newman, K. E. Thomas-Alyea, in *Electrochemical Systems Vol 3*, Aufl., Wiley-Interscience, Hoboken, NJ **2012**, p. s.l.
- [35] D. Guy, B. Lestriez, R. Bouchet, D. Guyomard, *J. Electrochem. Soc.* **2006**, 153, A679.
- [36] Y.-H. Chen, C.-W. Wang, G. Liu, X.-Y. Song, V. S. Battaglia, A. M. Sastry, *J. Electrochem. Soc.* **2007**, 154, A978.
- [37] R. Amin, Y.-M. Chiang, *J. Electrochem. Soc.* **2016**, 163, A1512.